

Structure from Articulated Motion: An Accurate and Stable Monocular 3D Reconstruction Approach without Training Data

Onorina Kovalenko¹ Vladislav Golyanik² Jameel Malik^{1,3,4} Ahmed Elhayek⁵ Didier Stricker^{1,4}

¹DFKI ²MPI for Informatics ³NUST-SEECS ⁴TU Kaiserslautern ⁵University of Prince Mugrin

Abstract

Recovery of articulated 3D structure from 2D observations is a challenging computer vision problem with many applications. Current learning-based approaches achieve state-of-the-art performance on public benchmarks but are limited to the specific types of objects and motions covered by the training datasets. Model-based approaches do not rely on training data but show lower accuracy on public benchmarks. In this paper, we introduce a new model-based method called *Structure from Articulated Motion (SfAM)*. SfAM includes a new articulated structure term which ensures consistency of bone lengths throughout the whole image sequence and recovers a scene-specific configuration of the articulated structure. The proposed approach is highly robust to noisy 2D annotations, generalizes to arbitrary objects and motion types and does not rely on training data. It achieves state-of-the-art accuracy and scales across different scenarios which is shown in extensive experiments on public benchmarks and real video sequences.

1. Introduction

3D structure recovery of articulated objects (*i.e.*, comprising multiple connected rigid parts) from a set of 2D point tracks through multiple monocular images is a challenging computer vision problem [50, 62, 70, 34]. Articulated structure recovery is ill-posed due to missing information about the third dimension [32]. Its applications include gesture and activity recognition, character animation in movies and games, motion analysis in sport and robotics.

Recently, multiple learning-based approaches which recover 3D structures from 2D landmarks have been introduced [26, 69, 41, 40]. These methods are restricted to a specific kind of structure (*e.g.*, human skeleton) and require extensive datasets for training. Moreover, they often fail to recover poses which are different from the training examples (see Sec. 4.2.3). When a scene includes different types of articulated objects, different methods have to be applied to reconstruct the whole scene.

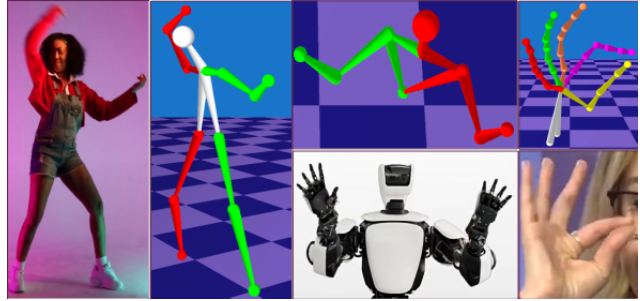


Figure 1: We recover different articulated structures from real-world videos with high accuracy and no need for training data. Our SfAM approach is not restricted to a single object class and only requires a rough articulated structure prior. The reconstructions are provided under different view angles.

In this paper, we introduce a general approach for accurate recovery of 3D structure and poses of any articulated structure from 2D observations which does not rely on training data (see Fig. 1). We build upon the recent progress in non-rigid structure from motion (NRSfM) which is a general technique for non-rigid 3D reconstruction from 2D point tracks. However, when considering an articulated object as a general non-rigid one, reconstructions can evince significant variation in the distances between the connected joints (see Sec. 4.5). These distances have to remain nearly constant across all articulated poses. Our method relies on this assumption and introduces a spatiotemporal constraint on the bone lengths.

We call our approach *Structure from Articulated Motion (SfAM)*. The core novelty of our method is the **articulated prior term** which automatically recovers canonical bone proportions of the observed structure. We rely on the assumption that bone lengths — though not known in advance — must remain the same across all frames. Nevertheless, our articulated structure term is a soft constraint which can cope with small observed deviations in the bone lengths. Starting from a rough initialization of the articulated structure (*e.g.*, a human arm can be longer than a leg), SfAM still converges to the correct structure proportions (see Sec. 4.5). Fig. 2 illustrates the significant difference between results produced by a general-purpose NRSfM technique [7] and

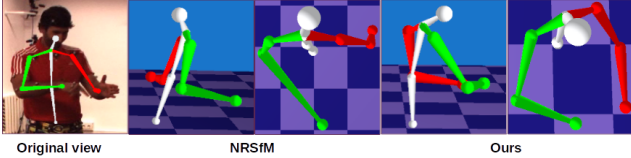


Figure 2: Side-by-side comparison of NRSfM method [7] and our SfAM. Reconstruction results of [7] look reasonable from the original camera view but violate anthropometric properties of human skeleton due to changing bone lengths from frame to frame.

our approach. To summarise, our **contributions** are:

- **A generic framework** for articulated structure recovery which achieves state-of-the-art accuracy across multiple datasets and is not restricted to specific objects (see Sec. 4). In contrast to most methods which achieve state-of-the-art results, our method does not require training data or known bone lengths.
- The **articulated prior energy term** which recovers sequence-specific bone proportions (see Sec. 3) and makes our approach robust to noisy 2D observations (see Sec. 4.4).

We demonstrate the effectiveness of SfAM for the recovery of different articulated structures through extensive quantitative and qualitative evaluation on different datasets [27, 6, 59] and real-world scenes (see Sec. 4). As a side effect of our method, it can be used for precise articulated model estimation (generate personalized human skeleton rigs (see Sec. 4.5)). This contrasts a lot with most recent supervised learning approaches which require extensive labeled databases for training, and still, often fail when unfamiliar poses are observed (see Sec. 4.2.3). Moreover, minor changes in the inputs lead to significant variations in the poses, which makes the results of learning-based methods very difficult or impossible to reproduce.

2. Related Work

Rigid and Non-Rigid Structure from Motion.

Factorization-based Structure from Motion (SfM) is a general technique for 3D structure recovery from 2D point tracks. SfM problem is well-posed for rigid objects due to the rigidity constraint [58]. Early extensions of Tomasi and Kanade’s method [58] for the non-rigid case rely on rank and orthonormality constraints [12, 11]. Subsequent methods investigated shape basis priors [65], temporal smoothness priors [8], trajectory space constraints [5] as well as such fundamental questions as shape basis uniqueness [25, 4]. More recent methods combine priors in the metric and trajectory spaces [24]. To improve the reconstruction of stronger non-linear deformations, Zhu *et al.* [72] introduce unions of linear subspaces. Dai *et al.* [18] propose an NRSfM method with as few additional constraints as possible. Since lately, the focus of NRSfM research is drawn to the problem of scalability [22, 7, 30],

i.e., the consistent performance across different scenarios and linear computational complexity in the number of points. Our SfAM is a scalable approach which builds upon the work of Ansari *et al.* [7]. In contrast to [7], we recover articulated structures with higher accuracy.

Articulated and Multibody Structure from Motion.

Over the last years, several SfM approaches for articulated motion were proposed. Some of them relax the global rigidity constraint for multiple parts [47, 16] so that each of the parts is constrained to be rigid. They can handle relatively simple articulated motions, as the segmentation and the structure composition are assumed to be unknown [47]. As a result, these methods are hardly applicable to such complicated scenarios as human and hand pose recovery. Tresadern and Reid [60], Yan and Pollefeys [67] and Palladini *et al.* [47] address the articulated case with two rigid body parts and detect a hinge joint. Later, an approach with spatial smoothness and segmentation dealing with an arbitrary number of rigid parts was proposed by Fayad *et al.* [20]. Next, Valmadre *et al.* [61] propose a dynamic-programming approach for the reconstruction of articulated 3D trees from input 2D joint positions operating in linear time. Multibody SfM methods reconstruct multiple independent rigid body transformations and non-rigid deformations in the same scene [16, 31]. In contrast, our approach is more general as it imposes a soft constraint of articulated motion on top of classic NRSfM.

Piecewise and Locally Rigid Structure from Motion.

Piecewise rigid approaches interpret the structure as locally rigid in the spatial domain [56, 21]. Several methods divide the structure into patches, each of which can deform non-rigidly [19, 33]. High granularity level of operation allows these methods to reconstruct large deformations as opposed to methods relying on linear low-rank subspace models [19]. Lee *et al.* [33] recover human motion by taking advantage of spatiotemporal segmentation of the point tracks. Rehan *et al.* [51] penalize deviations between the bone lengths (which have to stay rigid) from the average distances between the joints over the whole sequence. This form of constraint does not guarantee a realistic reconstruction though, as it struggles to compensate for inaccurate initializations or 3D inaccuracies in short time intervals.

Monocular 3D Human Body and Hand Pose Estimation.

Bone length constraints are widely used in the single-view regression of 3D human poses. One of the early works in this domain operates on single uncalibrated images and imposes constraints on the relative bone lengths [55]. It is capable of reconstructing a human pose up to scale. Later, an enhancement for multiple frames with bone symmetry and rigidity constraints (joints representing the same bone move rigidly relative to each other) was introduced by Wei and Chai [64]. Akhter and Black [3] use a pose prior that

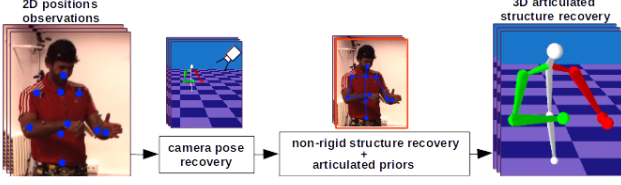


Figure 3: Pipeline of the proposed SfAM approach. Following factorization-based NRSfM, we first recover the camera pose using 2D position observations. Then, we recover 3D articulated structure by optimizing our new energy functional accounting for articulated priors.

captures pose-dependent joint angle limits. Ramakrishna *et al.* [50] use a sum of squared bone lengths term which can still lead to unrealistic poses. Wandt *et al.* constrain the bone lengths to be invariant [62]. Their trilinear factorization approach relies on pre-trained body poses serving as a shape prior and transcendental functions modeling periodic motion peculiar to the human gait. An adaptation of this approach to hand gestures would require the acquisition of a new shape prior. One of the recent methods for human pose and appearance estimation is MonoPerfCap of Xu *et al.* [66]. It imposes implicit bone length constraints through a dense template tailored to a specific person and captured in an external acquisition process.

Recently, many learning-based approaches for human pose and hand pose estimation have been presented in the literature [53, 28, 48, 42, 40, 37, 38]. These methods are highly specialized and rely on large collections of training data. In contrast, our SfAM is a general approach which can cope with different articulated structures, with no need for labeled datasets.

3. The Proposed SfAM Approach

Fig. 3 shows a high-level overview of our approach. factorization-based NRSfM, we first recover the camera pose using 2D landmarks (Sec. 3.2). For 3D structure recovery, we extend the target energy function of [7, 18] by our articulated prior term (Sec. 3.3.1). We assume that sparse 2D correspondences are given and propose a soft constraint on articulated motion with the advantage of the robustness to inaccurate initialization of bone proportions. In Sec. 3.3.2, we show how our new energy is efficiently optimized alternating between *fixed-point continuation algorithm* [36] and *Levenberg-Marquardt* [35, 39]. This leads to an accurate reconstruction of articulated motions of different structures.

3.1. Factorization Model

The input to SfAM is the measurement matrix $\mathbf{W} = [\mathbf{W}_1, \mathbf{W}_2, \dots, \mathbf{W}_T]^T \in \mathbb{R}^{2T \times N}$ with N 2D joints tracked over T frames. Every \mathbf{W}_t , $t \in \{1, \dots, T\}$, is registered to the centroid of the observed structure and the translation is resolved in advance. Since the intrinsic camera ma-

trix is not known in the case of an uncalibrated monocular setting, we use an orthographic camera model. Following standard SfM approaches, we assume that every 2D projection \mathbf{W}_t can be factorized into a camera pose-projection matrix $\mathbf{R}_t \in \mathbb{R}^{2 \times 3}$ and 3D structure $\mathbf{S}_t \in \mathbb{R}^{3 \times N}$ so that $\mathbf{W}_t = \mathbf{R}_t \mathbf{S}_t$. We assume that the articulated structure deforms in accordance with the low-rank shape model [12, 7]. Thus, $\mathbf{S} = [\mathbf{S}_1, \mathbf{S}_2, \dots, \mathbf{S}_T]^T$ can be parametrised by the set of unknown basis shapes $\mathbf{B} \in \mathbb{R}^{3K \times N}$ of cardinality K and the coefficient matrix $\mathbf{C} \in \mathbb{R}^{T \times K}$:

$$\mathbf{W} = \mathbf{R}\mathbf{S} = \mathbf{R} \underbrace{(\mathbf{C} \otimes \mathbf{I}_3)}_{\mathbf{M}} \mathbf{B} = \mathbf{M}\mathbf{B}, \quad (1)$$

where $\mathbf{R} = \text{bkdiag}(\mathbf{R}_1, \mathbf{R}_2, \dots, \mathbf{R}_T)$ is the joint camera pose-projection matrix, \mathbf{I}_3 is a 3×3 identity matrix and \otimes denotes Kronecker product.

3.2. Recovery of Camera Poses

Applying singular value decomposition to \mathbf{W} , we obtain initial estimates of \mathbf{M} and \mathbf{B} from (1) up to an invertible corrective transformation $\mathbf{Q} \in \mathbb{R}^{3K \times 3K}$:

$$\mathbf{W} \cong \mathbf{M}'\mathbf{B}' \cong \underbrace{\mathbf{M}'\mathbf{Q}}_{\mathbf{M}} \underbrace{\mathbf{Q}^{-1}\mathbf{B}'}_{\mathbf{B}} = \mathbf{M}\mathbf{B}. \quad (2)$$

In the following, we are using the shortcuts $\mathbf{M}'_{2t-1:2t} \in \mathbb{R}^{2 \times 3K}$ for every t -th pair of rows of \mathbf{M} , $\mathbf{Q}_k \in \mathbb{R}^{3K \times 3}$ for the k -th column triplet of \mathbf{Q} , $k \in \{1, \dots, K\}$. Considering (1) and (2), for every $t \in \{1, \dots, T\}$ and $k \in \{1, \dots, K\}$, we have:

$$\mathbf{M}'_{2t-1:2t} \mathbf{Q}_k = c_{tk} \mathbf{R}_t. \quad (3)$$

Using the orthonormality constraints $\mathbf{R}_t \mathbf{R}_t^T = \mathbf{I}_2$ and denoting $\mathbf{F} = \mathbf{Q}\mathbf{Q}^T$, we obtain:

$$\begin{cases} \mathbf{M}'_{2t-1} \mathbf{F}_k \mathbf{M}'_{2t-1}^T = \mathbf{M}'_{2t} \mathbf{F}_k \mathbf{M}'_{2t}^T = c_{ik}^2 \mathbf{I}_2, \\ \mathbf{M}'_{2t-1} \mathbf{F}_k \mathbf{M}'_{2t}^T = 0. \end{cases} \quad (4)$$

Therefore, the following systems of equations can be written for every t and k :

$$\underbrace{\begin{bmatrix} \mathbf{M}'_{2t-1} \otimes \mathbf{M}'_{2t-1}^T - \mathbf{M}'_{2t} \otimes \mathbf{M}'_{2t}^T \\ \mathbf{M}'_{2t-1} \otimes \mathbf{M}'_{2t}^T \end{bmatrix}}_{\mathbf{G}_t} \text{vec}(\mathbf{F}_k) = 0, \quad (5)$$

where $\text{vec}(\cdot)$ is vectorization operator permuting a $m \times n$ matrix to a mn column vector. Stacking all \mathbf{G}_t vertically, we obtain:

$$\mathbf{G} \text{vec}(\mathbf{F}_k) = 0, \quad (6)$$

where $\mathbf{G} = [\mathbf{G}_1, \mathbf{G}_2, \dots, \mathbf{G}_T]^T$. Finding an optimal \mathbf{F}_k can be performed by solving the optimization problem:

$$\min_{\mathbf{F}_k} \|\mathbf{G} \text{vec}(\mathbf{F}_k)\|^2. \quad (7)$$

Due to the rank-3 constraint on every \mathbf{F}_k , this problem is solved by iterative shrinkage-thresholding (IST) method [9]. Once an optimal \mathbf{F} is found, the corrective transformation \mathbf{Q} is recovered by Cholesky decomposition. Using \mathbf{Q} , \mathbf{R} is recovered from Eqs. (1)–(4).

3.3. Articulated Structure Recovery

3.3.1 Articulated Structure Representation

Having found \mathbf{R} , we recover \mathbf{S} . Note that we optionally rely on an updated \mathbf{W} after the smooth shape trajectory step which imposes additional constraints on point trajectories and reduces the overall number of unknowns, please refer to [7] for more details. We rearrange the shape matrix \mathbf{S} to

$$\mathbf{S}^\# = \begin{bmatrix} X_{11} \dots X_{1N} & Y_{11} \dots Y_{1N} & Z_{11} \dots Z_{1N} \\ \vdots & \vdots & \vdots \\ X_{T1} \dots X_{TN} & Y_{T1} \dots Y_{TN} & Z_{T1} \dots Z_{TN} \end{bmatrix}, \quad (8)$$

where $(X_{tn}, Y_{tn}, Z_{tn}), n \in \{1, \dots, N\}$ is a 3D coordinate of each joint in \mathbf{S} . $\mathbf{S}^\#$ can be represented as:

$$\mathbf{S}^\# = [\mathbf{P}_x \mathbf{P}_y \mathbf{P}_z](\mathbf{I}_3 \otimes \mathbf{S}), \quad (9)$$

where $\mathbf{P}_x, \mathbf{P}_y, \mathbf{P}_z \in \mathbb{R}^{T \times 3N}$ are binary row selectors. We follow [7, 18] and represent the optimal non-rigid structure by:

$$\min_{\mathbf{S}} \|\mathbf{S}^\# \mathbf{\Pi}\|_*, \quad \text{s. t. } \mathbf{W} = \mathbf{R}\mathbf{S}, \quad (10)$$

where $\mathbf{\Pi} = (\mathbf{I} - \frac{1}{T}\mathbf{1}\mathbf{1}^\top)$ ($\mathbf{1}$ is a vector of ones) and $\|\cdot\|_*$ denotes the nuclear norm. Note that $\text{rank}(\mathbf{S}^\#) \leq K$, and the mean 3D component is removed from $\mathbf{S}^\#$. As shown in Fig. 2, non-rigid structures recovered by the optimization of (10) can have significant variations in bone lengths. This often leads to unrealistic poses and body proportions. Unlike general non-rigid structures, in articulated structures individual rigid parts or bones have constant lengths throughout the whole sequence. Moreover, all the bones follow constant proportions which we call *articulated priors*. We incorporate the articulated priors into the objective function (10) in the form of the following energy term:

$$\mathbf{E}_{BL}(\mathbf{S}) = \sum_{t=1}^T \sum_{b=1}^B e_{tb}(\mathbf{S}), \quad (11)$$

where $e_{tb}(\mathbf{S}) = (D_b^t - L_b)^2$ is an energy term for bone b and frame t , L_b is initial normalized bone length value of bone b . The normalization is done with respect to the sum of all initial bone lengths. $D_b^t = \|X_{a_b}^t - X_{c_b}^t\|_2$ is Euclidian distance between joints $X_{a_b}^t$ and $X_{c_b}^t$ connected by bone b , B is the number of bones of the articulated structure. Vectors $a = [X_{a_1}, X_{a_2}, \dots, X_{a_B}]$ and $c = [X_{c_1}, X_{c_2}, \dots, X_{c_B}]$ define the parent and child joints of bones respectively.

Unlike some previous works [49, 17, 3, 68, 69, 62], we do not require predefined bone lengths or proportions. By

applying the soft articulated prior term, our method recovers optimal sequence-specific proportions which minimize the energy:

$$\min_{\mathbf{S}} \left(\|\mathbf{S}^\#\|_* + \frac{\beta}{2} \mathbf{E}_{BL}(\mathbf{S}) \right), \quad \text{s. t. } \mathbf{W} = \mathbf{R}\mathbf{S}, \quad (12)$$

where β is a scalar weight. Implementation of articulated prior term (11) in the form of a soft constraint makes the overall method robust to incorrect initialization of bone lengths.

3.3.2 Energy Optimization

Since (12) contains a non-linear term $\mathbf{E}_{BL}(\mathbf{S})$, we introduce an auxiliary variable \mathbf{A} and obtain the following optimization problem which is linear with respect to \mathbf{S} :

$$\begin{aligned} \min_{\mathbf{S}} \|\mathbf{S}^\#\|_* + \frac{\beta}{2} \min_{\mathbf{A}} \mathbf{E}_{BL}(\mathbf{A}), \\ \text{s. t. } \mathbf{W} = \mathbf{R}\mathbf{S} \text{ and } \mathbf{A} = \mathbf{S}. \end{aligned} \quad (13)$$

We rewrite (13) in the Lagrangian form:

$$\begin{aligned} \mathbf{L}(\mathbf{S}, \mathbf{A}, \mu) = \min_{\mathbf{S}} \mu \|\mathbf{S}^\#\|_* + \frac{\beta}{2} \mathbf{E}_{BL}(\mathbf{A}) \\ + \frac{1}{2} \|\mathbf{W} - \mathbf{R}\mathbf{S}\|_F^2 + \frac{1}{2} \|\mathbf{A} - \mathbf{S}\|_F^2, \end{aligned} \quad (14)$$

where $\|\cdot\|_F$ denotes the Frobenius norm and μ is a parameter. We split (14) into two subproblems:

$$\begin{aligned} \min_{\mathbf{S}} \mathbf{L}(\mathbf{S}, \mu) = \\ \min_{\mathbf{S}} \mu \|\mathbf{S}^\#\|_* + \frac{1}{2} \|\mathbf{W} - \mathbf{R}\mathbf{S}\|_F^2 + \frac{1}{2} \|\mathbf{A} - \mathbf{S}\|_F^2 \end{aligned} \quad (15)$$

$$\text{and } \min_{\mathbf{A}} \mathbf{L}(\mathbf{A}) = \frac{\beta}{2} \mathbf{E}_{BL}(\mathbf{A}) + \frac{1}{2} \|\mathbf{A} - \mathbf{S}\|_F^2. \quad (16)$$

We alternate between the subproblems (15) and (16) and iterate until convergence. \mathbf{A} remains fixed in (15) and \mathbf{S} remains fixed in (16). The subproblem (15) is linear and solved by the fixed-point continuation (FPC) method [36]. First, we obtain the gradient of $\frac{1}{2}(\|\mathbf{W} - \mathbf{R}\mathbf{S}\|_F^2 + \|\mathbf{A} - \mathbf{S}\|_F^2)$ with respect to $\mathbf{S}^\#$:

$$\begin{aligned} g(\mathbf{S}^\#, \mathbf{A}) = \frac{\partial \frac{1}{2}(\|\mathbf{W} - \mathbf{R}\mathbf{S}\|_F^2 + \|\mathbf{A} - \mathbf{S}\|_F^2)}{\partial \mathbf{S}^\#} = \\ [\mathbf{P}_x \mathbf{P}_y \mathbf{P}_z](\mathbf{I}_3 \otimes (\mathbf{R}^\top(\mathbf{R}\mathbf{S} - \mathbf{W}) + (\mathbf{S} - \mathbf{A}))). \end{aligned} \quad (17)$$

Next, FPC for $\min_{\mathbf{S}} \mathbf{L}(\mathbf{S}, \mu)$ instantiates as

$$\begin{aligned} \mathbf{Y}^{(t)} &= \mathbf{S}^{\#(t)} - \tau g(\mathbf{S}^{\#(t)}, \mathbf{A}^{(t)}), \\ \mathbf{S}^{\#(t+1)} &= \mathcal{S}_{\tau\mu^{(t)}}(\mathbf{Y}^{(t)}), \\ \mu^{(t+1)} &= \rho\mu^{(t)}, \end{aligned} \quad (18)$$

Algorithm 1 : Structure from Articulated Motion (SfAM)

Input: initial normalized bone lengths L_b , measurement matrix $\mathbf{W} \in \mathbb{R}^{2T \times N}$ with 2D point tracks

Output: poses $\mathbf{R} \in \mathbb{R}^{2T \times 3T}$ and 3D shapes $\mathbf{S} \in \mathbb{R}^{3T \times N}$

Initialize: $\mathbf{S}^{(0)}$ is initialized as in [7], $\mathbf{A}^{(0)} = \mathbf{S}^{(0)}$, $\beta = 1.5$, $\mu^{(0)} = 1$, $\rho = 0.25$, $\tau = 0.2$

step 1: recover \mathbf{R} with IST method [9] (Sec. 3.2)

step 2 (optional): smooth point trajectories in \mathbf{W} [7]

step 3: while not converged do

1: $\mathbf{A}^{(t+1)} = \arg \min_{\mathbf{A}} \left(\frac{\beta}{2} E_{BL}(\mathbf{A}) + \frac{1}{2} \|\mathbf{S}^{(t)} - \mathbf{A}\|_F^2 \right)$
(optimize with Levenberg-Marquardt [35, 39])

2: $g^{(t+1)} = \mathbf{R}^\top (\mathbf{R} \mathbf{S}^{(t)} - \mathbf{W}) + (\mathbf{S}^{(t)} - \mathbf{A}^{(t+1)})$

3: $\mathbf{Y}^{(t+1)} = \mathbf{S}^{(t)} - \tau g^{(t+1)}$

4: $\mathbf{S}^{(t+1)} = \mathcal{S}_{\tau \mu^{(t)}}(\mathbf{Y}^{(t+1)})$

5: $\mu^{(t+1)} = \mu^{(t)} \rho$

end while

where $\mathcal{S}_\nu(\cdot)$ is the matrix shrinkage operator [36] and $\tau > 0$ is a free parameter.

The second subproblem (16) is nonlinear and is optimized for each iteration (18) using Levenberg-Marquardt of *ceres* [1]. Let denote the r_l , $l \in \{1, \dots, TN\}$ residuals of $\frac{1}{2} \|\mathbf{A} - \mathbf{S}\|_F^2$. We aggregate all residuals $e_{tb}(\mathbf{A})$ from (11)¹ and r_l into a single function

$$\mathbf{F}(\mathbf{A}) = [e_{11}(\mathbf{A}), \dots, e_{BT}(\mathbf{A}), r_1, \dots, r_{TN}]^\top : \mathbb{R}^{3TN} \rightarrow \mathbb{R}^{BT+TN}. \quad (19)$$

Next, the objective function (16) can be compactly written in terms of \mathbf{A} as

$$\mathbf{L}(\mathbf{A}) = \|\mathbf{F}(\mathbf{A})\|_2^2. \quad (20)$$

The target non-linear energy optimization problem consists of finding an optimal parameter set \mathbf{A}' so that:

$$\mathbf{A}' = \arg \min_{\mathbf{A}} \|\mathbf{F}(\mathbf{A})\|_2^2. \quad (21)$$

We solve (21) iteratively. In every optimization step k , the objective is linearized in the vicinity of the current solution \mathbf{A}_k by the first-order Taylor expansion:

$$\mathbf{F}(\mathbf{A}_k + \Delta \mathbf{A}) \approx \mathbf{F}(\mathbf{A}_k) + \mathbf{J}(\mathbf{A}_k) \Delta \mathbf{A}, \quad (22)$$

with $\mathbf{J}(\mathbf{A})_{(BT+TN) \times 3TN}$ being the Jacobian of $\mathbf{F}(\mathbf{A}_k)$. For every iteration, the objective for $\Delta \mathbf{A}$ reads:

$$\min_{\Delta \mathbf{A}} \|\mathbf{J}(\mathbf{A}_k) \Delta \mathbf{A} + \mathbf{F}(\mathbf{A}_k)\|_2^2. \quad (23)$$

In *ceres* [1], the optimum is computed in the least-squares sense with Levenberg-Marquardt method:

$$[\mathbf{J}(\mathbf{A}_k)^\top \mathbf{J}(\mathbf{A}_k) + \lambda_k \mathbf{I}] \Delta \mathbf{A} = -\mathbf{J}(\mathbf{A}_k)^\top \mathbf{F}(\mathbf{A}_k), \quad (24)$$

where $\lambda_k > 0$ is a parameter and \mathbf{I} is an identity matrix. The algorithm is summarized in Alg. 1.

¹note that \mathbf{S} in (11) is substituted by \mathbf{A}

4. Experiments and Results

We extensively evaluate our SfAM on several datasets including Human 3.6m [27], synthetic sequences of Akhter *et al.* [6] and NYU hand pose [59] dataset. Moreover, we demonstrate qualitative results on challenging community videos. In total, our SfAM is compared to over twenty state-of-the-art model-based and learning-based methods (see Tables 1 and 2).

Human 3.6m [27] is currently the largest dataset for monocular 3D human pose sensing. It is widely used for evaluation of learning-based human pose estimation methods. We consider recent learning-based methods [53, 28, 45, 17, 42, 40, 48, 29, 57, 54] which achieve state-of-the-art results on Human 3.6m [27]. Some methods require 2D landmarks as input [42, 40, 41], while others use RGB images directly [53, 54, 45, 28].

Synthetic sequences of Akhter *et al.* [6] are commonly used for the evaluation of sparse NRSfM. We compare our approach to state-of-the-art methods including Metric Projections (MP) [46], Point Trajectory Approach (PTA) [5], both Column Space Fitting approaches (CSF1 and CSF2) [23, 24], Block Matrix Method (BMM) [18], the method of Lee *et al.* [33], Probabilistic Point Trajectory Approach (PPTA) [2] and Scalable Monocular Surface Reconstruction (SMSR) of Ansari *et al.* [7] which is the most related approach to our SfAM. This method was not evaluated on datasets for articulated motions [27, 59] before. Therefore, we implement SMSR and evaluate it on Human 3.6m [27] as well as community videos. Moreover, we extend SMSR [7] with the local rigidity constraint of Rehan *et al.* [51] and include it into our comparison.

For evaluation on datasets with provided 3D ground truth annotations, bone lengths are initialized with the average values for the subjects from the corresponding datasets. For community videos, bone lengths are initialized with the values from anthropometric data tables [13]. In all experiments we use a sliding time window of 200 frames. For sequences shorter than 200 frames, we run our method on the whole sequence at once. All experiments are performed on a system with 32 GB RAM and twelve-core Intel Xeon CPU running at 3.6GHz. Our framework is implemented in C++. Average processing time for a single frame from the Human 3.6m dataset [27] with given 2D annotations amounts to 140 *ms*.

In Sec. 4.2.3, we highlight the numerous cases when our method performs better than state-of-the-art learning-based approaches in real-world scenes. In Sec. 4.4, we evaluate the robustness of our approach to inaccuracies in 2D landmarks. Finally, the proposed SfAM recovers correct articulated structures given highly inaccurate initial bone lengths in Sec. 4.5.

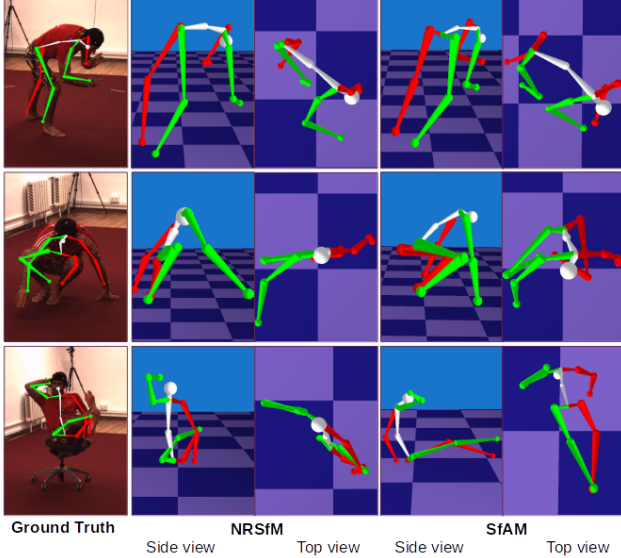


Figure 4: Comparison of our SfAM and NRSfM [7] on Human 3.6m [27]. NRSfM considers humans as general non-rigid objects and changes bone lengths from frame to frame.

4.1. Evaluation Methodology

We follow the established evaluation methodology in the area of NRSfM and rigidly align our 3D reconstructions to the ground truth. We report the reconstruction error \mathcal{E}_{3D} in *mm* between ground truth joint positions $\bar{\mathbf{S}}_n^t$ and aligned 3D reconstructions $G(\mathbf{S}_n^t)$:

$$\mathcal{E}_{3D} = \min_G \frac{1}{T} \frac{1}{N} \sum_{t=1}^T \sum_{n=1}^N \|\bar{\mathbf{S}}_n^t - G(\mathbf{S}_n^t)\|_2, \quad (25)$$

where $n \in \{1, \dots, N\}$, $t \in \{1, \dots, T\}$, T is the number of frames in the sequence and N is the number of joints of the articulated object. For some datasets, we report the normalized mean 3D error:

$$e_{3D} = \min_G \frac{1}{\sigma T} \frac{1}{N} \sum_{t=1}^T \sum_{n=1}^N \|\bar{\mathbf{S}}_n^t - G(\mathbf{S}_n^t)\|_2^2, \text{ with} \quad (26)$$

$$\sigma = \min_G \frac{1}{3T} \sum_{t=1}^T (\sigma_{tx} + \sigma_{ty} + \sigma_{tz}),$$

where σ_{tx} , σ_{ty} and σ_{tz} denote normalized variances of reconstructions $G(\mathbf{S}_n^t)$ along the x , y , z -axes respectively.

4.2. Human Pose Estimation

4.2.1 Human 3.6m Dataset

Table 1 gives an overview of the quantitative results on the Human 3.6m [27]. For all methods, we report the reconstruction error \mathcal{E}_{3D} after the rigid alignment of the recovered structures with ground truth. We highlight approaches

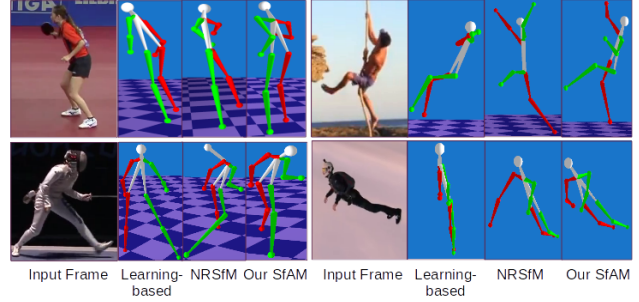


Figure 5: Comparison of our SfAM, NRSfM [7] and the learning-based method of Martinez *et al.* [40] on challenging real-world videos.

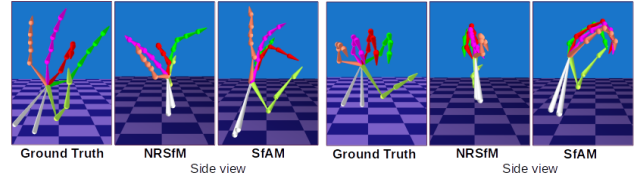


Figure 6: Comparison of our SfAM to NRSfM [7] on NYU hand pose dataset [59].

which are trained on Human 3.6m [27] with “*”. We follow three common evaluation protocols. In **Protocol #1**, we compare the methods on two subjects ($S9$ and $S11$). The original framerate 50 fps is reduced to 10 fps . The learning-based approaches marked with “*” use subjects $S1$, $S5$, $S6$, $S7$, $S8$ and all camera views for training. Testing is done for all cameras. For **Protocol #2**, only the frontal view (“camera3”) is used for evaluation. For **Protocol #3**, evaluation is done on every 64^{th} frame of subject $S11$ for all cameras. The learning-based approaches marked with “*” use subjects $S1$, $S5$, $S6$, $S7$, $S8$ and $S9$ for training.

As we see from Table 1, our approach achieves state-of-the-art performance. Moreover, we show competitive accuracy to best performing learning-based approaches [40, 48, 29, 54, 57, 53] which are trained on Human 3.6m [27]. In Sec. 4.2.3, we demonstrate that our approach works better in real-world scenes which are different from this dataset. Table 1 also shows that inclusion of our articulated energy term improves the accuracy by 52% compared to SMSR [7]. In Fig. 4, we visualize several reconstructions of highly challenging scenes by SMSR [7] and the proposed SfAM. See Fig. 8 for additional visualizations.

4.2.2 Synthetic NRSfM Datasets

We compare our approach with previous SfM methods on challenging synthetic sequences with a large variety of human motions *Drink*, *Pickup*, *Stretch*, *Yoga* [5]. Some pairs of joints remain locally rigid in these sequences. We activate the articulated constraint for those points and evaluate our method. Table 2 shows the results of SfAM and pre-

Method	Dir	Disc	Eat	Greet	Phone	Pose	Purch	Sit	SiTD	Smoke	Photo	Wait	Walk	WalkD	WalkT	Avg
Protocol #1																
Zhou <i>et al.</i> [70]*	99.7	95.8	87.9	116.8	108.3	93.5	95.3	109.1	137.5	106.0	107.3	102.2	110.4	106.5	115.2	106.7
Kanazawa <i>et al.</i> [28]*	-	-	-	-	-	-	-	-	-	-	-	-	-	-	-	67.5
Moreno-Noguer [42]*	53.5	50.5	65.8	62.5	56.9	60.6	50.8	56.0	79.6	63.7	80.8	61.8	59.4	68.5	62.1	62.2
Omran <i>et al.</i> [45]*	-	-	-	-	-	-	-	-	-	-	-	-	-	-	-	59.9
Zhou <i>et al.</i> [71]*	46.7	47.7	54.9	54.1	56.3	46.9	49.1	60.1	81.5	53.2	65.4	49.7	47.1	54.2	53.7	54.7
Mehta <i>et al.</i> [41]*	-	-	-	-	-	-	-	-	-	-	-	-	-	-	-	54.6
Pavlakos <i>et al.</i> [49]*	47.5	50.5	48.3	49.3	50.7	46.1	48.0	61.1	78.1	51.1	55.2	48.3	41.5	52.9	46.4	51.9
Kinauer <i>et al.</i> [29]*	-	-	-	-	-	-	-	-	-	-	-	-	-	-	-	50.3
Tekin <i>et al.</i> [57]*	-	-	-	-	-	-	-	-	-	-	-	-	-	-	-	50.1
Rogez <i>et al.</i> [53]*	-	-	-	-	-	-	-	-	-	-	-	-	-	-	-	49.2
Martinez <i>et al.</i> [40]*	37.4	42.3	45.2	44.6	49.3	40.7	37.6	54.9	63.1	47.4	54.6	44.7	35.2	47.3	39.6	45.6
Pavlakos <i>et al.</i> [48]*	34.7	39.8	41.8	38.6	42.5	38.0	36.6	50.7	56.8	42.6	47.5	39.6	32.1	43.9	36.5	41.8
Dabral <i>et al.</i> [17]*	28.0	30.7	39.1	34.4	37.1	28.9	31.2	39.3	60.6	39.3	44.8	31.1	25.3	37.8	28.4	36.3
SMSR[7]	91.9	115.9	113.3	110.0	107.1	91.1	113.2	140.8	156.6	101.0	117.8	88.0	68.2	98.5	84.1	106.6
SMSR[7]+[51]	128.9	145.7	150.1	129.6	143.6	130.4	146.9	172.4	176.1	141.2	164.5	136.4	130.4	145.9	135.9	145.2
Our SfAM	43.0	45.2	53.2	44.6	48.0	41.2	66.4	59.0	88.2	47.9	42.1	45.3	49.1	50.8	44.1	51.2
Protocol #2																
Akhter <i>et al.</i> [3]	199.2	177.6	161.8	197.8	176.2	195.4	167.3	160.7	173.7	177.8	186.5	181.9	198.6	176.2	192.7	181.1
Ramakrishna <i>et al.</i> [50]	137.4	149.3	141.6	154.3	157.7	141.8	158.1	168.6	175.6	160.4	158.9	161.7	174.8	150.0	150.2	157.3
Bogo <i>et al.</i> [10]	62.0	60.2	67.8	76.5	92.1	73.0	75.3	100.3	137.3	83.4	77.0	77.3	86.8	79.7	81.8	82.3
Kanazawa <i>et al.</i> [28]*	-	-	-	-	-	-	-	-	-	-	-	-	-	-	-	66.5
Rogez <i>et al.</i> [53]*	-	-	-	-	-	-	-	-	-	-	-	-	-	-	-	51.1
SMSR[7]	97.6	113.0	108.4	107.9	105.1	92.4	112.3	138.0	155.2	98.5	119.5	88.6	67.4	96.3	78.0	105.2
SMSR[7]+[51]	121.5	136.2	160.2	120.0	128.9	135.4	142.1	165.6	159.2	102.6	128.8	101.6	72.0	105.2	90.2	124.0
Our SfAM	43.8	45.5	53.6	45.8	47.4	42.6	66.7	57.2	87.7	47.8	44.5	45.6	50.4	50.0	46.3	51.7
Protocol #3																
Yasin <i>et al.</i> [68]	88.4	72.5	108.5	110.2	97.1	81.6	107.2	119.0	170.8	108.2	142.5	86.9	92.1	165.7	102.0	110.2
Rogez <i>et al.</i> [52]	-	-	-	-	-	-	-	-	-	-	-	-	-	-	-	88.1
Chen, Ramanan [15]*	71.6	66.6	74.7	79.1	70.1	67.6	89.3	90.7	195.6	83.5	93.3	71.2	55.7	85.9	62.5	82.7
Nie <i>et al.</i> [44]*	62.8	69.2	79.6	78.8	80.8	72.5	73.9	96.1	106.9	88.0	86.9	70.7	71.9	76.5	73.2	79.5
Sun <i>et al.</i> [54]*	-	-	-	-	-	-	-	-	-	-	-	-	-	-	-	48.3
Rogez <i>et al.</i> [53]*	-	-	-	-	-	-	-	-	-	-	-	-	-	-	-	42.7
SMSR[7]	96.9	110.2	110.9	108.6	109.2	88.5	109.7	129.1	145.2	95.7	110.0	90.2	75.9	90.5	73.5	102.9
SMSR[7]+[51]	134.2	135.6	152.2	128.3	136.2	126.5	140.6	166.9	170.7	113.5	152.3	136.4	124.6	145.1	135.1	139.9
Our SfAM	47.4	40.1	54.0	44.7	49.6	40.6	70.9	61.4	89.8	48.3	41.4	47.3	54.7	60.8	53.8	53.6

Table 1: The reconstruction error \mathcal{E}_{3D} of SfAM and previous methods on Human 3.6m dataset. "*" indicates learning-based methods which are trained on Human3.6m [27]. We outperform all model-based approaches and reach very close to the tuned supervised learning techniques.

Method	Drink	PickUp	Stretch	Yoga
MP [46]	0.4604	0.4332	0.8549	0.8039
PTA [5]	0.0250	0.2369	0.1088	0.1625
CSF1 [23]	0.0223	0.2301	0.0710	0.1467
CSF2 [24]	0.0223	0.2277	0.0684	0.1465
BMM [18]	0.0266	0.1731	0.1034	0.1150
Lee [33]	0.8754	1.0689	0.9005	1.2276
PPTA [2]	0.011	0.235	0.084	0.158
SMSR [7]	0.0287	0.2020	0.0783	0.1493
SMSR[7]+[51]	0.4348	0.4965	0.3721	0.4471
Our SfAM	0.0226	0.1921	0.0673	0.1242

Table 2: The normalized mean 3D error e_{3D} of previous NRSfM methods and our SfAM for synthetic sequences [5].

vious SfM methods. The errors e_{3D} for other listed methods are taken from PPTA [2] and Ansari *et al.* [7]. Only PPTA [2] outperforms SfAM on *Drink*, whereas CSF2 [24] achieves a comparable e_{3D} . SfAM achieves the most consistent performance among all compared algorithms.

4.2.3 Real-World Videos

Our algorithm is capable of recovering human motion from challenging real-world videos. We compare our results with the state-of-the-art learning-based approach of Martinez *et al.* [40] and one of the best performing general-purpose

NRSfM methods SMSR [7]. Since ground truth 2D annotations are not available, we use OpenPose [14] for 2D human body landmark extraction. As Fig. 5 shows, [40] fails to correctly recover poses which are different from the training dataset [27]. SMSR [7] produces unrealistic human body structures. In contrast to [40, 7], our method successfully recovers 3D human poses in real-world scenes.

4.3. Hand Pose Estimation

We also evaluate SfAM on the NYU hand pose dataset [59] which provides 2D and 3D ground truth annotations for 8252 different hand poses. The hand model consists of 30 bones. Hand pose recovery is a challenging problem due to occlusion and many degrees of freedom. We compare the performance of our approach with SMSR [7] and its modification with local rigidity constraint from Rehan *et al.* [51]. Quantitatively, SfAM achieves \mathcal{E}_{3D} of 14.2 mm. In contrast, \mathcal{E}_{3D} of SMSR [7] is 22.2 mm, and SMSR with articulated body constraints [51] shows \mathcal{E}_{3D} of 19.4 mm. Hence, the inclusion of our articulated prior term to [7] achieves an error improvement of 56%. The qualitative results are shown in Fig. 6. Similar to human bodies, SfAM achieves lower error due to keeping bone lengths constant between frames. When SMSR [7] fails to reconstruct the correct 3D pose, SfAM still outputs plausible results.

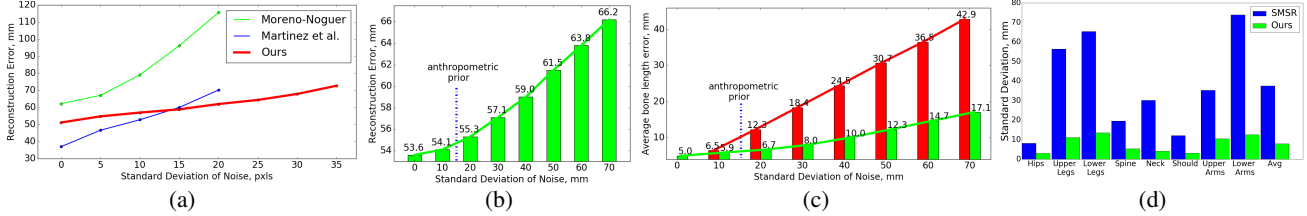


Figure 7: (a): The reconstruction error e_{3D} under 2D noise. (b): e_{3D} under incorrect bone lengths initializations. (c): Average bone lengths error for the increasing levels of Gaussian noise before (red) and after (green) the optimization. (d): Standard deviation of bone lengths for SMSR [7] and our SfAM.

4.4. Robustness to Inaccurate 2D Point Tracks

We validate the robustness of our approach to inaccuracies in 2D landmarks on Human 3.6m [27]. We compare our SfAM to state-of-the-art learning-based methods [42, 40] trained on ground truth 2D data. We add Gaussian noise with increasing values of the standard deviation to the 2D ground truth point tracks. The reconstruction error as the function of the standard deviation of the noise is plotted in Fig. 7(a). SfAM is more robust than the compared methods for moderate and high perturbations, and the error grows very slowly with the increasing noise level. In contrast to our SfAM, the errors of [42, 40] grow very fast even with a low level of noise. Note that we evaluate our method on a higher level of noise than [42, 40]. The average error of the currently best performing 2D detectors is between 10-15 pixels [63, 43]. We see that for 10-15 pixels, SfAM has comparable error to the most accurate learning-based approaches while not relying on training data and being generalizable for different object classes.

4.5. Robustness to Incorrectly Initialized Bone Lengths and Real Bone Length Recovery

We study the accuracy of SfAM in recovering articulated structures given incorrectly initialized bone proportions (normalized bone lengths) on the subject S11 from Human 3.6m [27]. Starting from the ground truth initialization of bone lengths (obtained from the dataset), we change every bone length by adding different amounts of Gaussian noise with increasing standard deviations in the range $[0; 70]$ mm. This allows us to analyse the recovered bone lengths and the robustness of SfAM to noise in a controlled and well-defined setting. The results of the experiment are plotted in Fig. 7(b). If the structure is initialized with anthropometric priors from [13], the error increases by only 3%. Note that our error in bone length estimation is slightly affected by the increasing levels of noise. It is equal to 54 mm with ground truth initialization and grows just to 66 mm with $\sigma = 70$ mm. Note that the anthropometric prior corresponds to $\sigma \approx 15$ mm.

Given incorrect initial bone lengths, SfAM recovers not only correct poses but also accurate sequence-specific bone lengths. We calculate the average difference between

ground truth bone lengths of subject S11 and the initial ones, provided to our method. We do the same for the recovered structures. The results are best viewed in Fig. 7(c). Thus, SfAM can be used for precise skeleton estimation.

We also calculate standard deviations of bone lengths of the reconstructed objects for SMSR [7] and SfAM. Fig. 7(d) shows that the standard deviation of bone lengths is very high for SMSR [7], as it considers a human as a general non-rigid object and changes the bone lengths from frame to frame. SfAM reduces the average standard deviation by 514% leading to a more accurate pose reconstruction and structure recovery. In Fig. 7(d), "Upper Legs" and "Lower Legs" denote bones between the hip/knee and knee/ankle respectively; "Upper Arms" and "Lower Arms" denote bones between shoulder/elbow and elbow/wrist respectively.

5. Conclusion

We present a new method for 3D articulated structure recovery from 2D landmarks. The proposed approach is general and not restricted to specific structures or motions. Integration of our soft articulated prior term into general-purpose NRSfM approach and alternating optimization resulted in accurate and stable results.

In contrast to the vast majority of state-of-the-art approaches, our method does not require training data or known bone lengths. By ensuring consistency of bone lengths throughout the whole sequence, our SfAM optimizes sequence-specific bone proportions and recovers 3D structures. In extensive experiments, it proves its generalizability and shows state-of-the-art accuracy on public benchmarks. It also shows a remarkable improvement in accuracy compared to other model-based approaches. Moreover, our method outperforms learning-based approaches in complicated real-world videos. All in all, we show that state-of-the-art accuracy on benchmarks can be achieved without the need for training and parameter tuning for specific datasets.

In future work, we are planning to apply our SfAM as a component for animal shape estimation and recovery of personalized human skeletons. We also plan to use our approach to boost the development of approaches for human and hand pose estimation with semi-supervision.

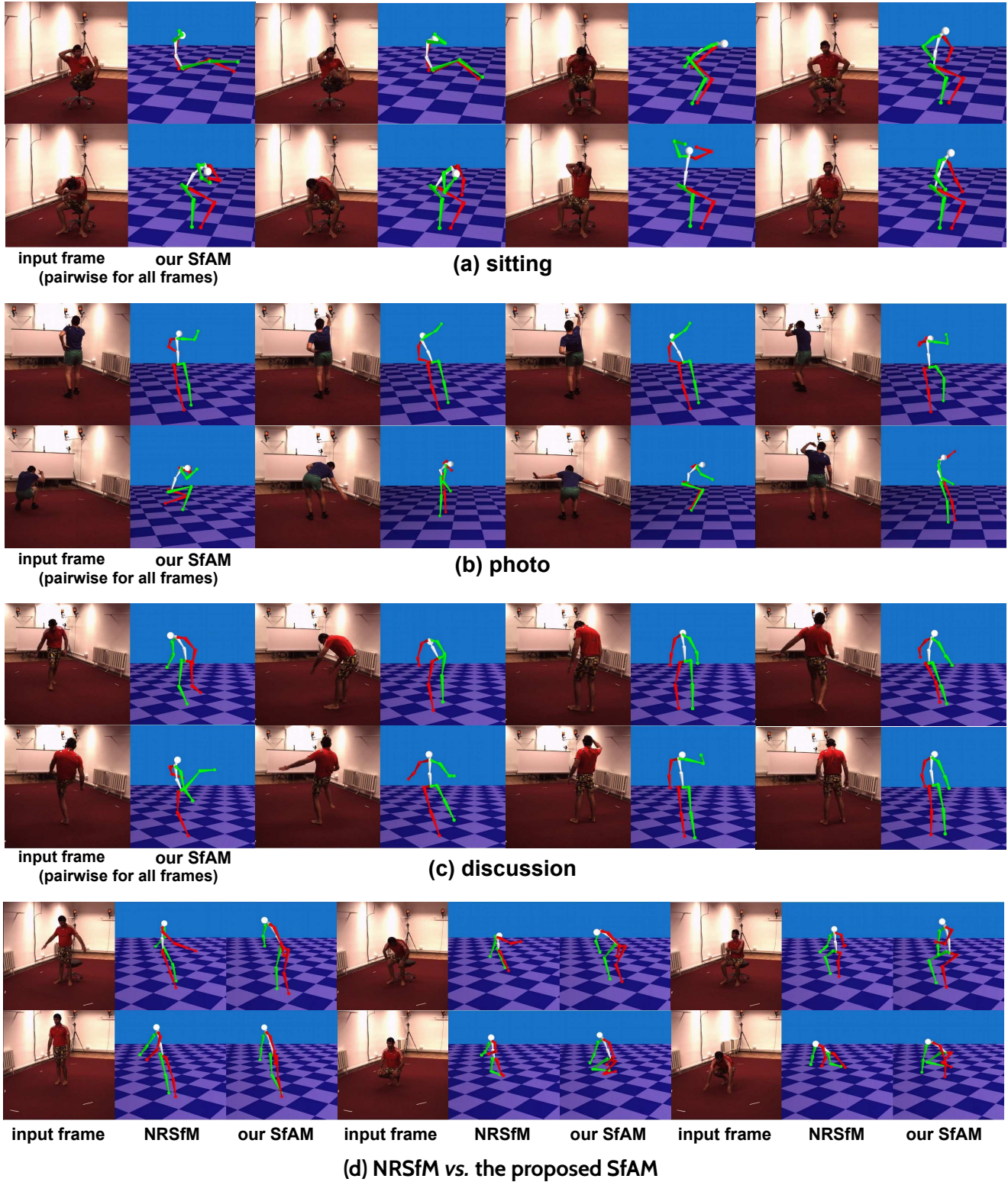


Figure 8: Additional visualizations of our results and reconstructions with NRSfM of Ansari *et al.* [7] on several sequences from [27]. (a)-(c): Our results on *sitting*, *photo* and *discussion*. These sequences and poses are among the most challenging in the dataset. (d): Comparison of our SfAM and NRSfM [7].

Acknowledgement

This work was funded by the project VIDETE (grant number 01IW18002) of the German Federal Ministry of Education and Research (BMBF).

References

- [1] S. Agarwal, K. Mierle, and Others. Ceres solver. <http://ceres-solver.org>. 5
- [2] A. Agudo and F. Moreno-Noguer. A scalable, efficient, and accurate solution to non-rigid structure from motion. *Computer Vision and Image Understanding (CVIU)*, pages 121–133, 2018. 5, 7
- [3] I. Akhter and M. J. Black. Pose-conditioned joint angle limits for 3d human pose reconstruction. In *Computer Vision and Pattern Recognition (CVPR)*, 2015. 2, 4, 7
- [4] I. Akhter, Y. Sheikh, and S. Khan. In defense of orthonormality constraints for nonrigid structure from motion. In *Computer Vision and Pattern Recognition (CVPR)*, pages 1534–1541, 2009. 2
- [5] I. Akhter, Y. Sheikh, S. Khan, and T. Kanade. Nonrigid structure from motion in trajectory space. In *Advances in Neural Information Processing Systems (NIPS)*, pages 41–48, 2008. 2, 5, 6, 7
- [6] I. Akhter, Y. Sheikh, S. Khan, and T. Kanade. Trajectory space: A dual representation for nonrigid structure from motion. *IEEE Transactions on Pattern Analysis and Machine Intelligence (TPAMI)*, pages 1442–1456, 2011. 2, 5
- [7] M. Ansari, V. Golyanik, and D. Stricker. Scalable dense monocular surface reconstruction. In *3D Vision (3DV)*, 2017. 1, 2, 3, 4, 5, 6, 7, 8, 9
- [8] A. Bartoli, V. Gay-Bellile, U. Castellani, J. Peyras, S. Olsen, and P. Sayd. Coarse-to-fine low-rank structure-from-motion. In *Computer Vision and Pattern Recognition (CVPR)*, 2008. 2
- [9] A. Beck and M. Teboulle. A fast iterative shrinkage-thresholding algorithm for linear inverse problems. *SIAM Journal on Imaging Sciences*, pages 183–202, 2009. 4, 5
- [10] F. Bogo, A. Kanazawa, C. Lassner, P. V. Gehler, J. Romero, and M. J. Black. Keep it SMPL: automatic estimation of 3d human pose and shape from a single image. In *European Conference on Computer Vision (ECCV)*, pages 561–578, 2016. 7
- [11] M. Brand. A direct method for 3d factorization of nonrigid motion observed in 2d. In *Computer Vision and Pattern Recognition (CVPR)*, pages 122–128, 2005. 2
- [12] C. Bregler, A. Hertzmann, and H. Biermann. Recovering non-rigid 3d shape from image streams. In *Computer Vision and Pattern Recognition (CVPR)*, pages 690–696, 2000. 2, 3
- [13] C. C. Gordon, T. Churchill, C. E. Clauser, B. Bradtmiller, and J. T. McConville. Anthropometric survey of u.s. army personnel: Methods and summary statistics 1988. page 649, 09 1989. 5, 8
- [14] Z. Cao, T. Simon, S.-E. Wei, and Y. Sheikh. Realtime multi-person 2d pose estimation using part affinity fields. In *Computer Vision and Pattern Recognition (CVPR)*, 2017. 7
- [15] C. Chen and D. Ramanan. 3d human pose estimation = 2d pose estimation + matching. In *Computer Vision and Pattern Recognition (CVPR)*, pages 5759–5767, 2017. 7
- [16] J. P. Costeira and T. Kanade. A multibody factorization method for independently moving objects. *International Journal of Computer Vision (IJCV)*, pages 159–179, 1998. 2
- [17] R. Dabral, A. Mundhada, U. Kusupati, S. Afaque, A. Sharma, and A. Jain. Learning 3d human pose from structure and motion. In *European Conference on Computer Vision (ECCV)*, pages 679–696, 2018. 4, 5, 7
- [18] Y. Dai, H. Li, and M. He. A simple prior-free method for non-rigid structure-from-motion factorization. *International Journal of Computer Vision (IJCV)*, pages 101–122, 2014. 2, 3, 4, 5, 7
- [19] J. Fayad, L. Agapito, and A. Del Bue. Piecewise quadratic reconstruction of non-rigid surfaces from monocular sequences. In *European Conference on Computer Vision (ECCV)*, pages 297–310, 2010. 2
- [20] J. Fayad, C. Russell, and L. Agapito. Automated articulated structure and 3d shape recovery from point correspondences. In *International Conference on Computer Vision (ICCV)*, pages 431–438, 2011. 2
- [21] V. Golyanik, A. Jonas, and D. Stricker. Consolidating segmentwise non-rigid structure from motion. In *International Conference on Machine Vision Applications (MVA)*, 2019. 2
- [22] V. Golyanik and D. Stricker. Dense batch non-rigid structure from motion in a second. In *Winter Conference on Applications of Computer Vision (WACV)*, pages 254–263, 2017. 2
- [23] P. F. U. Gotardo and A. M. Martínez. Kernel non-rigid structure from motion. In *International Conference on Computer Vision (ICCV)*, pages 802–809, 2011. 5, 7
- [24] P. F. U. Gotardo and A. M. Martínez. Non-rigid structure from motion with complementary rank-3 spaces. In *Computer Vision and Pattern Recognition (CVPR)*, pages 3065–3072, 2011. 2, 5, 7
- [25] R. Hartley and R. Vidal. Perspective nonrigid shape and motion recovery. In *European Conference on Computer Vision (ECCV)*, 2008. 2
- [26] M. R. I. Hossain and J. J. Little. Exploiting temporal information for 3d human pose estimation. In *European Conference on Computer Vision (ECCV)*, pages 69–86, 2018. 1
- [27] C. Ionescu, D. Papava, V. Olaru, and C. Sminchisescu. Human3.6m: Large scale datasets and predictive methods for 3d human sensing in natural environments. *IEEE Transactions on Pattern Analysis and Machine Intelligence (TPAMI)*, 36(7):1325–1339, 2014. 2, 5, 6, 7, 8, 9
- [28] A. Kanazawa, M. J. Black, D. W. Jacobs, and J. Malik. End-to-end recovery of human shape and pose. In *Computer Vision and Pattern Recognition (CVPR)*, pages 7122–7131, 2018. 3, 5, 7
- [29] S. Kinauer, R. A. Güler, S. Chandra, and I. Kokkinos. Structured output prediction and learning for deep monocular 3d human pose estimation. In *Energy Minimization Methods in Computer Vision and Pattern Recognition (EMMCVPR)*, pages 34–48, 2017. 5, 6, 7

- [30] S. Kumar, A. Cherian, Y. Dai, and H. Li. Scalable dense non-rigid structure-from-motion: A grassmannian perspective. In *Computer Vision and Pattern Recognition (CVPR)*, 2018. 2
- [31] S. Kumar, Y. Dai, and H. Li. Spatio-temporal union of subspaces for multi-body non-rigid structure-from-motion. *Pattern Recognition*, 2017. 2
- [32] H.-J. Lee and Z. Chen. Determination of 3d human body postures from a single view. *Computer Vision, Graphics, and Image Processing (ICVGIP)*, 1985. 1
- [33] M. Lee, J. Cho, and S. Oh. Consensus of non-rigid reconstructions. In *Computer Vision and Pattern Recognition (CVPR)*, pages 4670–4678, 2016. 2, 5, 7
- [34] S. Leonardos, X. Zhou, and K. Daniilidis. Articulated motion estimation from a monocular image sequence using spherical tangent bundles. In *International Conference on Robotics and Automation (ICRA)*, pages 587–593, 2016. 1
- [35] K. Levenberg. A method for the solution of certain non-linear problems in least squares. *Quarterly of Applied Mathematics*, 2(2):164–168, jul 1944. 3, 5
- [36] S. Ma, D. Goldfarb, and L. Chen. Fixed point and bregman iterative methods for matrix rank minimization. *Math. Program.*, pages 321–353, 2011. 3, 4, 5
- [37] J. Malik, A. Elhayek, F. Nunnari, K. Varanasi, K. Tamaddon, A. Heloir, and D. Stricker. Deephps: End-to-end estimation of 3d hand pose and shape by learning from synthetic depth. *3D Vision (3DV)*, 2018. 3
- [38] J. Malik, A. Elhayek, and D. Stricker. Simultaneous hand pose and skeleton bone-lengths estimation from a single depth image. In *3D Vision (3DV)*, pages 557–565, 2017. 3
- [39] D. W. Marquardt. An algorithm for least-squares estimation of nonlinear parameters. 11(2):431–441, 1963. 3, 5
- [40] J. Martinez, R. Hossain, J. Romero, and J. J. Little. A simple yet effective baseline for 3d human pose estimation. In *International Conference on Computer Vision (ICCV)*, pages 2659–2668, 2017. 1, 3, 5, 6, 7, 8
- [41] D. Mehta, H. Rhodin, D. Casas, P. Fua, O. Sotnychenko, W. Xu, and C. Theobalt. Monocular 3d human pose estimation in the wild using improved CNN supervision. In *3D Vision (3DV)*, pages 506–516, 2017. 1, 5, 7
- [42] F. Moreno-Noguer. 3d human pose estimation from a single image via distance matrix regression. In *Computer Vision and Pattern Recognition (CVPR)*, pages 1561–1570, 2017. 3, 5, 7, 8
- [43] A. Newell, K. Yang, and J. Deng. Stacked hourglass networks for human pose estimation. In *European Conference on Computer Vision (ECCV)*, 2016. 8
- [44] B. X. Nie, P. Wei, and S. Zhu. Monocular 3d human pose estimation by predicting depth on joints. In *International Conference on Computer Vision (ICCV)*, pages 3467–3475, 2017. 7
- [45] M. Omran, C. Lassner, G. Pons-Moll, P. V. Gehler, and B. Schiele. Neural body fitting: Unifying deep learning and model based human pose and shape estimation. In *3D Vision (3DV)*, pages 484–494, 2018. 5, 7
- [46] M. Paladini, A. Del Bue, M. Stosic, M. Dodig, J. M. F. Xavier, and L. Agapito. Factorization for non-rigid and articulated structure using metric projections. In *Computer Vision and Pattern Recognition (CVPR)*, pages 2898–2905, 2009. 5, 7
- [47] M. Paladini, A. Del Bue, J. Xavier, L. Agapito, M. Stosic, and M. Dodig. Optimal metric projections for deformable and articulated structure-from-motion. *International Journal of Computer Vision (IJCV)*, pages 252–276, 2012. 2
- [48] G. Pavlakos, X. Zhou, and K. Daniilidis. Ordinal depth supervision for 3D human pose estimation. In *Computer Vision and Pattern Recognition (CVPR)*, 2018. 3, 5, 6, 7
- [49] G. Pavlakos, X. Zhou, K. G. Derpanis, and K. Daniilidis. Coarse-to-fine volumetric prediction for single-image 3D human pose. In *Computer Vision and Pattern Recognition (CVPR)*, 2017. 4, 7
- [50] V. Ramakrishna, T. Kanade, and Y. Sheikh. Reconstructing 3d human pose from 2d image landmarks. In *European Conference on Computer Vision (ECCV)*, pages 573–586, 2012. 1, 3, 7
- [51] A. Rehan, A. Zaheer, I. Akhter, A. Saeed, B. Mahmood, M. Usmani, and S. Khan. Nrsfm using local rigidity. In *Winter Conference on Applications of Computer Vision (WACV)*, pages 69–74, 2014. 2, 5, 7
- [52] G. Rogez and C. Schmid. Mocap-guided data augmentation for 3d pose estimation in the wild. In *Advances in Neural Information Processing Systems (NIPS)*, pages 3108–3116, 2016. 7
- [53] G. Rogez, P. Weinzaepfel, and C. Schmid. LCR-Net++: Multi-person 2D and 3D Pose Detection in Natural Images. *IEEE Transactions on Pattern Analysis and Machine Intelligence (TPAMI)*, 2019. 3, 5, 6, 7
- [54] X. Sun, J. Shang, S. Liang, and Y. Wei. Compositional human pose regression. In *International Conference on Computer Vision (ICCV)*, pages 2621–2630, 2017. 5, 6, 7
- [55] C. J. Taylor. Reconstruction of articulated objects from point correspondences in a single uncalibrated image. *Computer Vision and Image Understanding (CVIU)*, pages 349–363, 2000. 2
- [56] J. Taylor, A. D. Jepson, and K. N. Kutulakos. Non-rigid structure from locally-rigid motion. In *Computer Vision and Pattern Recognition (CVPR)*, pages 2761–2768, 2010. 2
- [57] B. Tekin, P. Márquez-Neila, M. Salzmann, and P. Fua. Learning to fuse 2d and 3d image cues for monocular body pose estimation. In *International Conference on Computer Vision (ICCV)*, pages 3961–3970, 2017. 5, 6, 7
- [58] C. Tomasi and T. Kanade. Shape and motion from image streams under orthography: a factorization method. *International Journal of Computer Vision (IJCV)*, pages 137–154, 1992. 2
- [59] J. Tompson, M. Stein, Y. Lecun, and K. Perlin. Real-time continuous pose recovery of human hands using convolutional networks. *ACM Transactions on Graphics (ToG)*, 2014. 2, 5, 6, 7
- [60] P. Tresadern and I. Reid. Articulated structure from motion by factorization. In *Computer Vision and Pattern Recognition (CVPR)*, pages 1110–1115, 2005. 2
- [61] J. Valmadre, Y. Zhu, S. Sridharan, and S. Lucey. Efficient articulated trajectory reconstruction using dynamic programming and filters. In *European Conference on Computer Vision (ECCV)*, pages 72–85, 2012. 2

- [62] B. Wandt, H. Ackermann, and B. Rosenhahn. 3d reconstruction of human motion from monocular image sequences. *IEEE Transactions on Pattern Analysis and Machine Intelligence (TPAMI)*, (8):1505–1516, 2016. 1, 3, 4
- [63] S.-E. Wei, V. Ramakrishna, T. Kanade, and Y. Sheikh. Convolutional pose machines. *Computer Vision and Pattern Recognition (CVPR)*, 2016. 8
- [64] X. K. Wei and J. Chai. Modeling 3d human poses from uncalibrated monocular images. In *International Conference on Computer Vision (ICCV)*, pages 1873–1880, 2009. 2
- [65] J. Xiao, J.-x. Chai, and T. Kanade. A closed-form solution to non-rigid shape and motion recovery. In *European Conference on Computer Vision (ECCV)*, pages 573–587, 2004. 2
- [66] W. Xu, A. Chatterjee, M. Zollhöfer, H. Rhodin, D. Mehta, H.-P. Seidel, and C. Theobalt. Monoperfcap: Human performance capture from monocular video. *ACM Transactions on Graphics (ToG)*, 2018. 3
- [67] J. Yan and M. Pollefeys. A factorization-based approach for articulated nonrigid shape, motion and kinematic chain recovery from video. *IEEE Transactions on Pattern Analysis and Machine Intelligence (TPAMI)*, pages 865–877, 2008. 2
- [68] H. Yasin, U. Iqbal, B. Krüger, A. Weber, and J. Gall. 3d pose estimation from a single monocular image. *CoRR*, 2015. 4, 7
- [69] X. Zhou, Q. Huang, X. Sun, X. Xue, and Y. Wei. Towards 3d human pose estimation in the wild: A weakly-supervised approach. In *International Conference on Computer Vision (ICCV)*, pages 398–407, 2017. 1, 4
- [70] X. Zhou, M. Zhu, K. Derpanis, and K. Daniilidis. Sparseness meets deepness: 3d human pose estimation from monocular video. In *Computer Vision and Pattern Recognition (CVPR)*, 2016. 1, 7
- [71] X. Zhou, M. Zhu, G. Pavlakos, S. Leonardos, K. G. Derpanis, and K. Daniilidis. Monocap: Monocular human motion capture using a CNN coupled with a geometric prior. *IEEE Transactions on Pattern Analysis and Machine Intelligence (TPAMI)*, 2018. 7
- [72] Y. Zhu, D. Huang, F. D. la Torre Frade, and S. Lucey. Complex non-rigid motion 3d reconstruction by union of subspaces. In *Computer Vision and Pattern Recognition (CVPR)*, 2014. 2